Rock Mechanics and Rock Engineering (2021) 54:5761–5779
https://doi.org/10.1007/s00603-021-02586-w

ORIGINAL PAPER

Experimental Study on Mechanical Properties, Permeability and Acoustic Emission Characteristics of Gypsum Rock Under THM Coupling

Cheng Lyu[1] · Jianfeng Liu[1,2] · Zhide Wu[2] · Hejuan Liu[3] · Fukun Xiao[4] · Yin Zeng[1]

Received: 15 October 2020 / Accepted: 19 July 2021 / Published online: 2 August 2021

Abstract
The mechanical properties and permeability of gypsum caprock have a significant influence on the tightness and stability of salt cavern gas storage, a series of tests were carried out to investigate the mechanical properties, permeability and AE characteristics of gypsum under THM coupling in this work. The peak strength of gypsum increases with the increase of confining pressure and the decrease of temperature, the failure and dilatation failure criteria are obtained by utilizing Mogi failure criterion. The permeability decreases with the increase of temperature in the compaction and linear elastic deformation stage, and the final permeability decreases with the increase of temperature under the confining pressure of 5 MPa and 15 MPa, while increase with the increase of temperature under the confining pressure of 25 MPa and 35 MPa. And the permeability decreases with the increase of confining pressure in the whole test process because of the constrain of confining pressure on the formation of microcracks and pores. The best fitting formulas of the relationship between permeability and confining pressure is given by fitting at 25 °C and 110 °C, which can be expressed by two exponential functions. The AE characteristics also confirmed that the increase of confining pressure and temperature inhibited the formation of microcracks and pores, and the AE peaks have the same hysteresis effect as the stress peaks. It is noted that the peaks of AE ring count increase with the increase of temperature under the confining pressure of 35 MPa.

Keywords Permeability · Failure modes · Acoustic emission (AE) · Gypsum

Abbreviations

K	Permeability under THM coupling
μ	Dynamic viscosity coefficient of nitrogen
β	Compression coefficient of nitrogen
V	Volume of nitrogen in cylinders
Δt	Test time of permeability measurement
A	Cross-sectional area of the sample
L	Height of the sample
P0	Osmotic pressure difference at the initial moment
Pt	Osmotic pressure difference at the final moment
τoct	Octahedral shear stress of the stress space of the Mogi failure criterion
σm,2	Effective Mogi mean stress of the stress space of the Mogi failure criterion
σ1	First principal stresses under the triaxial test
σ2	Second principal stresses under the triaxial test
σ3	Third principal stresses under the triaxial test
$\tau_{oct}^{p}, \sigma_{m,2}^{p}$	Octahedral peak shear stress and corresponding effective principal stress
$\tau_{oct}^{d}, \sigma_{m,2}^{d}$	Octahedral dilatation shear stress and corresponding effective principal stress
$k_p^{T=25°C}$	Final permeability at T = 25 °C
$k_p^{T=110°C}$	Final permeability at T = 110 °C

✉ Jianfeng Liu
liujf@scu.edu.cn

[1] State Key Laboratory of Hydraulics and Mountain River Engineering, Sichuan University, Sichuan 610065, China

[2] CNPC Key Lab. of Oil and Gas Underground Storage Eng, Langfang 065007, China

[3] Institute of Rock and Soil Mechanics, Chinese Academy of Sciences, State Key Experiments in Geotechnical Mechanics and Engineering, Wuhan 430071, China

[4] Heilongjiang Ground Pressure & Gas Control in Deep Mining Key Laboratory, Heilongjiang University of Science and Technology, Harbin 150022, Heilongjiang, China

1 Introduction

Gypsum material plays an indispensable role in ensuring the tightness of oil/gas caverns because of its low permeability (Chen et al. 2017; Iucolano et al. 2018; Sarkar et al. 2019). Gypsum is a natural sulfate mineral, and its main component is hydrous calcium sulfate $CaSO_4{\cdot}2H_2O$ (Sarkar et al. 2019). The gypsum universally exists in salt cavern gas storage as a caprock or interlayer of salt rock, and reasonable evaluation of the permeability and mechanical properties of gypsum is conducive to evaluate the safety and tightness of salt cavern gas storage, which can avoid serious accidents caused by gas leakage (Wang et al. 2015). To evaluate the feasibility of salt cavern gas storage, Wang et al. (2015) obtained the interlayer and mudstone from Jintan salt mine of China for the test, and get the permeabilities and pores. Combined with numerical simulation, it was revealed that the permeability of the interlayer has a significant influence on gas seepage pressure of rock mass around the cavern and plays a key role in the tightness of salt cavern. Temperature and confining pressure have significant effects on the mechanical properties and permeability of rock materials (Hangx et al. 2011; Milsch et al. 2011; Olgaard et al. 1995). Olgaard et al. (1995) discussed the influence of gypsum dehydration reaction and solid volume reduction on permeability under different temperatures (23–150 °C), different confining pressures, different pore pressures, and different strain rates through laboratory experiments. When the test temperature exceeded the dehydration temperature, the strength of the rock decreases significantly, and the local brittle failure of the rock sample can be observed. Milsch et al. (2011) investigated the evolution of permeability caused by dehydration reaction of natural gypsum under ambient pressure and temperature of 293–423 K. The permeability increased with the progress of reaction, from about 7×10^{-19} to 3×10^{-16} m^2, indicating that dehydration reaction of gypsum has a significant effect on permeability. Hangx et al. (2011) investigated the mechanical behavior of anhydrite and the permeability characteristics of CO_2 in anhydrite at 20 and 80 °C. The experimental results of Leclère et al.(2018) shown that the permeability of gypsum sample remains low under high effective confining pressure, which slows the dehydration reaction rate at 115 °C. Wei et al. (2020) carried out triaxial compression tests of gypsum-like rock materials at different temperatures (45 and 220 °C), and the peak strength of samples increased with the increase of confining pressure. The strength of samples at 220 °C was obviously lower than that at 45 °C, and the samples shown obvious plastic softening characteristics due to high-temperature dehydration. Chaki et al. (2008) focused on the study of the influence of thermal damage at 200—600 ℃ on the physical properties of granite samples, including pore, permeability, and ultrasonic propagation. Tao et al. (2017) used a self-designed rock triaxial test system with high-temperature and high-pressure function to investigate the permeability and microstructure of gypsum at a constant hydrostatic pressure of 25 MPa and an increasing temperature (starting 20 °C to 650 °C). With a certain pore pressure, the curve of permeability with temperature can be divided into five stages according to the trends of permeability with temperature, and the maximum permeability measured by the test was no more than 10^{-17} m^2. Therefore, it is of great significance to understand the mechanical and permeability characteristics of gypsum caprock or interlayer under the thermal-hydro-mechanical (THM) coupling for the safety of salt cavern oil/gas storage. To reflect the internal deformation and failure of materials during the test, acoustic emission technology is undoubtedly one of the most reliable methods, which has been widely used in rock engineering (Wang et al. 2020; Zhao et al. 2020).

An AE event is an elastic wave released when a microcrack occurs in the internal structure of a material, which is widely used to investigate the failure mechanism of rocks or other materials (Wang et al. 2019b; Wei et al. 2019; Yang et al. 2012; Zhao et al. 2020). AE was first used by Obert in the monitoring of mine rockburst in the United States and has made satisfactory achievements with further development (Lockner 1993). In 1968, Scholz (1968) carried out a laboratory three-dimensional localization study for the first time. The AE waveforms from uniaxial loading to failure of granite samples were recorded, and the spatial location of each AE event was determined. To investigate the influence of stress anisotropy on the brittle failure of granite under uniaxial compression, Zang et al. (1998) conducted non-standard asymmetric compression tests on Aue granite and the test results showed that the maximum event density of asymmetric test doubled compared with the symmetric test. Meng et al. (2018) established the relationship among stress, strain, AE activity, cumulative AE activity and duration of 180 rock specimens under 36 cyclic loading, and discussed the AE characteristics of rock materials during deformation and failure under cyclic loading. It is demonstrated that AE characteristics are not only closely related to the stress–strain characteristics of rock materials but also significantly affected by the developmental state and degree of internal microcracks. Due to little research on the influence of environmental conditions on the damage of gypsum in stone, Menéndez et al. (2012) employed AE technology to monitor the elastic energy released during the salt crystallization cycles in limestone to quantify the damage caused by gypsum crystallization. It has been found that the AE activity under low relative humidity conditions is lower than the AE activity under high relative humidity conditions, and the

AE activity at room temperature is also lower than that under dry conditions at 50 °C. The experiment result of Brantut et al.(2012) indicated that the dehydration reaction at higher temperature is associated by a large number of AE events, which is due to the focal mechanisms of AE activity after the gypsum sample is compacted. Chen et al. (2017) performed a uniaxial compression AE test on gypsum and sandstone samples and obtained the load-axial deformation curve and the AE characteristic parameters during the whole fracture process of the specimen. Although the permeability and AE characteristics of various rocks have made great progress, what is not yet clear is the mechanical properties, permeability and AE properties of gypsum under thermal-hydro-mechanical coupling.

This thesis set out to further understand the mechanical properties, permeability and AE characteristics of gypsum caprock in deep salt cavern oil/gas storage under THM coupling, which can make up for the gaps of previous research. In the present work, the permeability tests of gypsum under triaxial loading with different temperatures and confining pressures were carried out by a self-designed THM multi-field coupled test system. According to the experimental results, the influence of confining pressure and temperature on the mechanical properties of gypsum has been discussed, and the evolution rule of permeability and AE characteristics of gypsum with different confining pressure and temperature was further explored, which can provide the theoretical basis for the construction of gas storage containing gypsum caprock or interlayer.

2 Experimental Method and Materials

2.1 Experimental Apparatus

The triaxial tests of gypsum samples were carried out using the MTS815 flex GT rock mechanics test system improved by Sichuan University and acoustic emission PCI-2 test system (Zhang et al. 2019). Figure 1 shows a schematic diagram of the experimental system. This test device is capable of simulating the gas permeation with different confining pressures and different temperatures. It has a maximum axial force of 4600 kN, maximum confining pressure of 140 MPa, the maximum gas pressure of 10 MPa, and test temperature can be set from room temperature to 200 °C. An axial extensometer with a measuring range of − 5 to 5 mm and a circumferential extensometer with a measuring range of − 2.5 to 8 mm are adopted to measure the axial and lateral deformations of gypsum samples (Zhang et al. 2019). The loading system controlled by computer, and then the data collection system automatically records the axial forces and confining pressures, inlet and outlet gas pressures, the transient flow rate of gas seepage, and the axial and circumferential deformations (Changbao Jiang 2017). As illustrated in Fig. 1, 8, AE sensors were set around the triaxial chamber, and PCI-2 AE system was employed to monitor and record the cracking process of gypsum samples in the whole test process. The corresponding sampling rate was fixed at 40 MSPS, the gain of signal amplifier and the threshold of AE acquisition system were 40 dB and 30 dB, respectively.

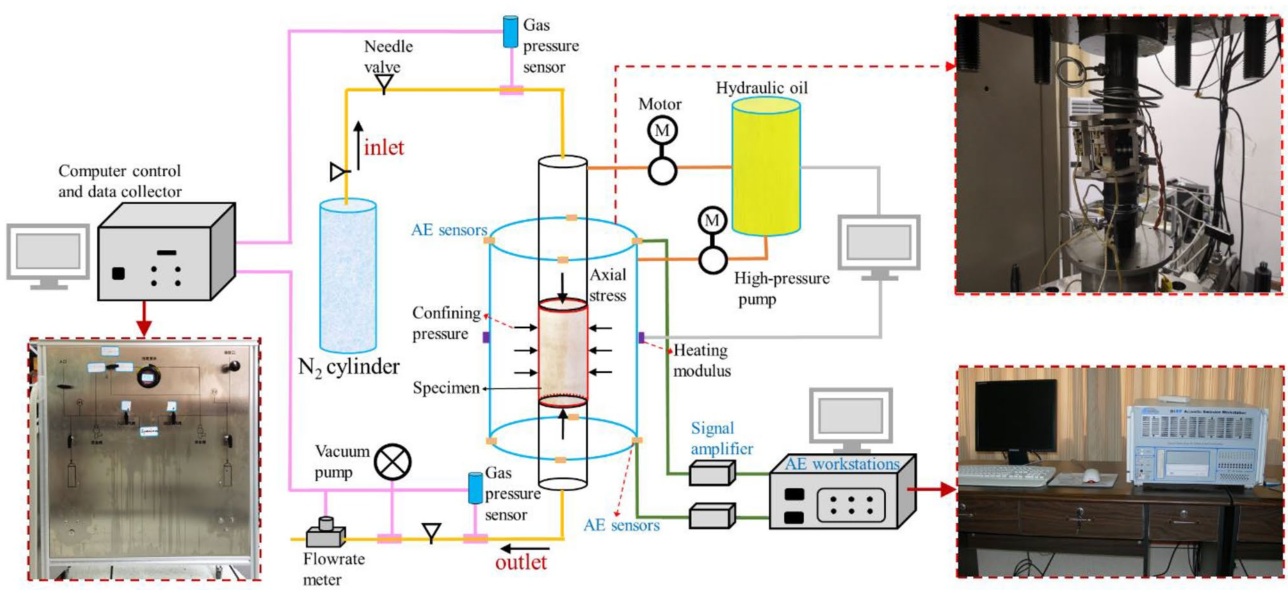

Fig.1 Improved rock THM test system **a** Gypsum samples **b** XRD pattern of gypsum samples **c** SEM observation of gypsum samples d) The molecular structure of $GaSO_4{\cdot}2H_2O$

2.2 Preparation of Gypsum Samples

The samples were collected from the caprock of a salt cavern gas storage from China, and then the gypsum samples were processed into standard samples with 38 mm in diameter and 76 mm in height according to the related standards (Feng et al. 2019). All gypsum samples tested are shown in Fig. 2(a), and the results of X-ray powder diffraction (XRD) are shown in Fig. 2(b), indicating that hydrous calcium sulfate $CaSO_4{\cdot}2H_2O$ is the major component of gypsum samples. Scanning electron microscope (SEM) imaging analysis (Fig. 2(c)) shows that the structure is closely arranged, and the pore of gypsum samples ranged from 0.233 to 0.75% using AP608 overburden osmometer (Yunpeng 2020). Figure 2(d) depicts the molecular structure of $CaSO_4{\cdot}2H_2O$, indicating that gypsum is a layered structure of SO_4^{2-} tetrahedron, in which two continuous layers are attached by Ca^{2+} ions, forming double sheet layers separated by water molecules (H_2O). Employing the orthogonal tests, the mechanical properties, permeability and AE characteristics of gypsum samples with different confining pressures and temperatures were systematically investigated, and the corresponding experimental conditions and the physical parameters of gypsum samples are given in Table 1 (Wang et al. 2019a; Zhang et al. 2019; Zhao et al. 2018). The gypsum samples were confined to a triaxial chamber at room temperature and confining pressure of 40 MPa for 24 h, which can eliminate the influence of initial damage and cracks on permeability and mechanical properties (Zhang et al. 2019).

2.3 Testing Scheme

All gypsum samples should be kept dry before the test, and the detailed experimental procedures are as follows::

(1) To prevent the hydraulic oil from entering the sample, the sample was wrapped with heat shrinking film and put into the triaxial chamber, and the axial and circumferential extensometers were installed. As shown in Fig. 1, the AE sensors were installed on the outer wall of the triaxial chamber and the AE test system was debugged.

(a) Gypsum samples

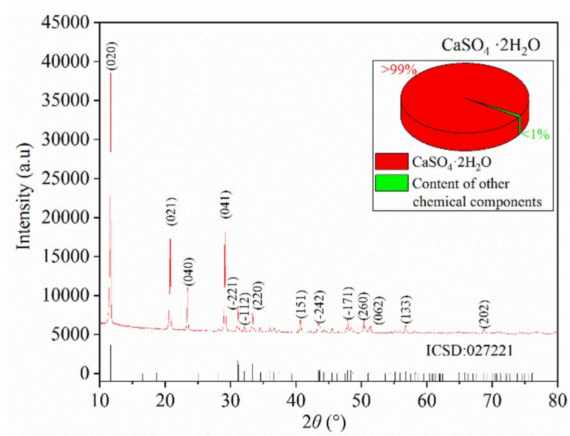

(b) XRD pattern of gypsum samples

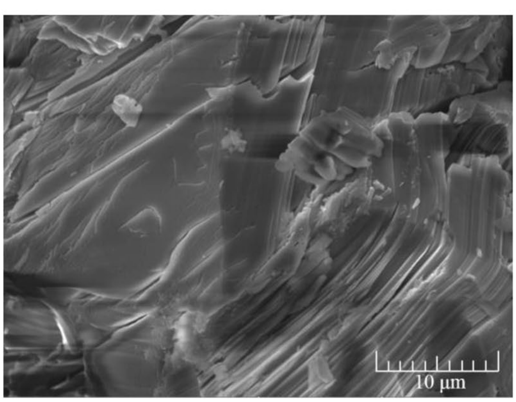

(c) SEM observation of gypsum samples

(d) The molecular structure of GaSO4·2H2O

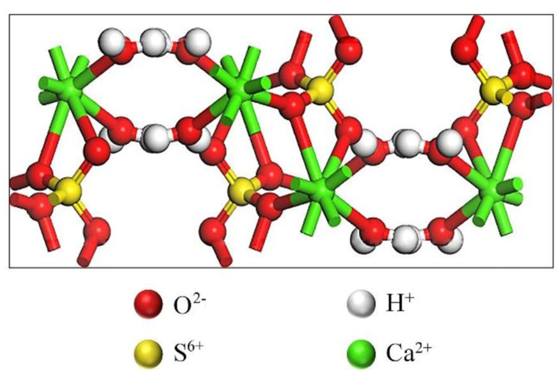

Fig. 2 Natural gypsum for testing **a** T = 25 °C **b** T = 60 °C **c** T = 110 °C

Table 1 The experimental conditions of gypsum samples

Specimen code	Confining (MPa)	Temperature (°)	Particle volume (cc)	Porosity (%)	Density (g/cm^3)
1	5	25	85.12	2.86	2.26
2	15	25	85.17	3.21	2.27
3	25	25	85.14	3.28	2.27
4	35	25	85.39	2.68	2.24
5	5	60	85.43	2.85	2.26
6	35	60	85.30	2.44	2.44
7	5	110	85.58	2.30	2.26
8	15	110	75.34	3.02	2.26
9	25	110	85.11	3.11	2.27
10	35	110	84.57	2.82	2.26

(2) After increasing the confining pressure to the target confining pressure (5, 15, 25 and 35 MPa) at a loading rate of 3 MPa/min, gas pressure was applied to both ends of the sample, and the pressure value was set to 1.5 MPa. The permeability obtained after the first test of the permeability of the gypsum sample was recorded as k_0.

(3) After the temperature was increased to the target temperature (60 °C and 110 °C) by the heating system at the heating rate of 0.5 °C/min, the heating system stopped upon heating and kept constant temperature for 3 h to make the sample heated evenly. After the insulation procedure was completed, the permeability was tested again, which was regarded as the permeability k_1 after heating.

(4) The loading rate was controlled to 0.08 mm/min by the linear variable differential transformer (LVDT), and the axial loading was carried out until the specimen was deformed or cracked. When the axial stress reached the anticipative stress point, the transient method was applied to test the permeability parameters at the stress point (Brace et al. 1968; Zhou et al. 2020). Each sample was tested more than ten times during the whole process of loading to failure, including once at the peak stress point and more than three times after the peak stress.

Referring to previous research, the calculation method of permeability is presented in the following equation (Brace et al. 1968; Zhou et al. 2020):

$$k = \mu\beta V \frac{\ln\left(P_0/P_t\right)}{2\Delta t \times (A/L)}, \tag{1}$$

where k is denoted as the permeability (m^2); μ represents the dynamic viscosity coefficient of nitrogen (1.8×10^{-5} Pa·s); β represents the compression coefficient of nitrogen; V means the volume of nitrogen in cylinders (m^3), $V = 500$ mL is substituted into Eq. (1) in this experiment; Δt is the duration of permeability measurement (s); A intends the cross-sectional area of the sample (m^2); L implies the height of the sample (m); P_0 and P_t are the osmotic pressure difference at the initial and final moment, respectively.

3 Experimental Results and Discussion

3.1 Analysis of Mechanical Properties

3.1.1 Stress–Strain Curves Under THM Coupling

A series of stress–strain curves of gypsum samples were obtained under the coupled action of THM with different confining pressures and temperatures. Figure 3 shows the full stress–strain curves of gypsum samples, which experiences compaction, linear elastic deformation, microcrack initiation, unstable crack growth, and macroscopic crack failure stages, under different temperatures and confining pressures (Shengqi et al. 2017; Zhang et al. 2019). It is found that temperature and confining pressure have a significant impact on the stress–strain curves of gypsum samples by comparing each curve in Fig. 3 (Brantut et al. 2011; Wang et al. 2019c). It is worth highlighting that the stress–strain curves of gypsum samples indicate stress concussion, which is consistent with published studies (Chiara et al. 2020; Hoxha et al. 2006). As illustrated in Fig. 3, the stress decreases for a short time, then increases, and then circulates until the failure of gypsum samples. This happened due to the low-temperature (T < 95 °C) experiment process, the destruction or dislocation slip of the crystal water particles occur in gypsum sample (Fig. 4), resulting in the stress decreases, and then the broken crystal water particles fill new pores, resulting in the stress rise. According to previous studies, gypsum samples will dehydrate when the temperature is higher than 95 °C as interpreted in Eq. (2) and Fig. 4, and most of the crystal water will be lost between 95 and 170 °C (Ko S 1995; Strydom C A 1995). When the temperature is 110 °C, most of the calcium sulfate dihydrate ($CaSO_4 \cdot 2H_2O$) turns into calcium sulfate

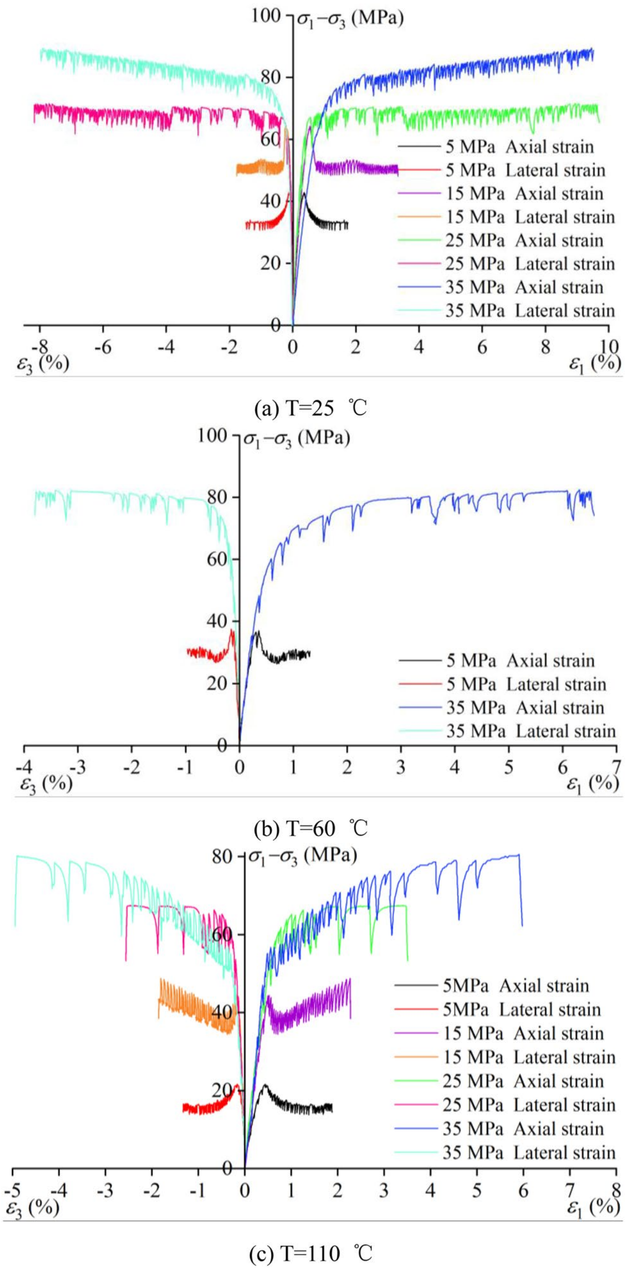

Fig. 3 Stress–strain curves of gypsum samples under THM coupling: The stress–strain curve shows a unique stress fluctuation phenomenon under THM coupling. When the confining pressure increases from 5 to 35 MPa, the peak strength of the sample increases continuously, and the deformation process of gypsum gradually changes from brittle deformation stage to brittle–ductile transition stage

hemihydrate ($GaSO_4{\cdot}0.5H_2O$), which leads to the increase of pores in gypsum samples, and the decrease of stress is more obvious than that at low temperature (T < 95 °C). Under the action of load, the new pores are filled by water crystals and the stress increase. The stress dropping increases with the increase of temperature due to the thermal expansion effect and dehydration reaction.

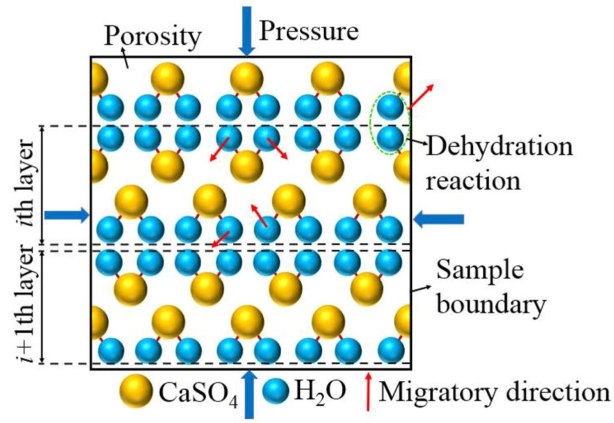

Fig. 4 The molecular structure of gypsum samples under THM coupling. During the experiment at low temperature (T < 95 °C), the crystal water particles in gypsum samples are destroyed or dislocated, and the broken crystal water particles fill new pores. When the temperature is higher than 95 °C, the gypsum sample will dehydrate, and most of the calcium sulfate dihydrate ($CaSO_4{\cdot}2H_2O$) will be converted into calcium sulfate hemihydrate ($CaSO_4{\cdot}0.5H_2O$)

$$CaSO_4 \cdot 2H_2O \rightarrow CaSO_4 \cdot 0.5H_2O + 1.5H_2O. \quad (2)$$

3.1.2 Strength Characteristics Under THM Coupling

As shown in Fig. 5, the determination of the characteristic stress of samples undergoing brittle and ductile deformation can refer to the studies of Cai et al. (2004) and Zhou et al. (2019). On the stress–strain curve in Fig. 5, σ_{cc}, σ_{ci}, σ_{cd} and σ_s represent the crack closure stress, crack initiation stress, dilatancy stress and peak strength, respectively. It should be emphasized that the peak strength of the specimen undergoing ductile deformation corresponds

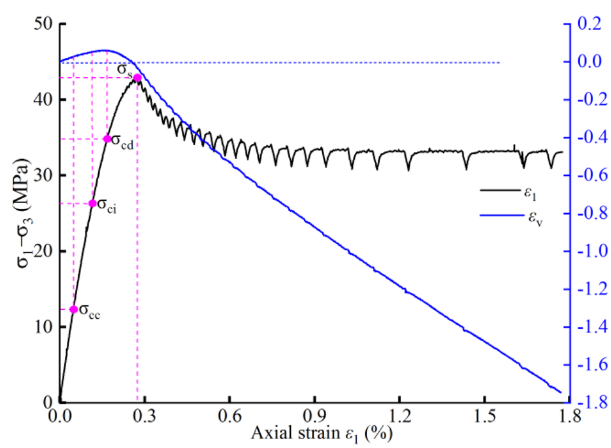

Fig. 5 Determination of characteristic damage stress

to the maximum deviatoric stress. The results of characteristic damage stresses and deformation parameters under THM coupling are shown in Table 2, and the relationship between characteristic stress and confining pressure at 25 °C and 110 °C can be well fitted by linear function, which is presented in Fig. 6(a), (b). With the increase of temperature or the decrease of confining pressure, the characteristic damage stress of gypsum sample decreases. According to Table 2, the elastic modulus and Poisson's ratio of gypsum increase with the increase of confining pressure and the decrease of temperature. The variation of elastic modulus and Poisson's ratio with confining pressure can be well fitted by linear function, which is shown in Fig. 6(c), (d). When the temperature increases from 25 to 110 °C, the elastic modulus decreases by 50.7% ~ 58.4%, and the Poisson's ratio decreases by 0 ~ 44.0%. Thus, the confining pressure and temperature have significant effects on the elastic modulus and Poisson's ratio of gypsum under THM coupling.

Table 2 and Fig. 6 show the peak strength σ_s of different temperature and confining pressure, and reveals that the peak strength σ_s increases with the increase of confining pressure, but decreases with the increase of temperature. As the temperature increases, the crystal water particles of the gypsum sample are destroyed. The higher the temperature, the more crystal water is lost, and more internal pores are formed, which leads to a decrease in strength (Mirwald 2008). With the confining pressure of 5 MPa and 35 MPa, the peak strength σ_s at 60 °C decreased by 14.1% and 5.3% compared with that at 25 °C, while the peak strength σ_s at 110 °C decreased by 49.8% and 7.8%, respectively, compared with that at 25 °C.

To more accurately evaluate the strength of gypsum under the triaxial test, we adopt the Mogi failure criterion, which is more preferable than the traditional Mohr–Coulomb failure criterion (Hangx et al. 2010; Mogi 1971). This can better analyze the experimental data of gypsum samples, thereby helping to investigate the mechanical behavior of the caprock of the salt cavern gas storage. The Mogi stress state is usually applied to describe the strength of rock under triaxial test, which can be expressed as

$$\tau_{oct} = \frac{1}{3}\sqrt{\left(\sigma_1 - \sigma_2\right)^2 + \left(\sigma_2 - \sigma_3\right)^2 + \left(\sigma_3 - \sigma_1\right)^2} \tag{3}$$

$$\sigma_{m,2} = \frac{\sigma_1 + \sigma_3}{2}, \tag{4}$$

where τ_{oct} and $\sigma_{m,2}$ are defined as the octahedral shear stress and effective Mogi mean stress of the stress space of the Mogi failure criterion, respectively. σ_1 、σ_2 and σ_3 represent the principal stresses when rock failure under the triaxial test. In our experiments $\sigma_2 = \sigma_3$, then Eq.(3) can be converted to

$$\tau_{oct} = \frac{\sqrt{2}}{3}\left(\sigma_1 - \sigma_3\right). \tag{5}$$

According to the Mogi failure criterion and our experimental data, the corresponding octahedral space stress can be obtained, including octahedral peak shear stress τ^p_{oct} and corresponding effective principal stress $\sigma^p_{m,2}$, octahedral dilatation shear stress τ^d_{oct} and corresponding effective principal stress $\sigma^d_{m,2}$. By fitting the experimental data at 25 °C and 110 °C shown in Fig. 7, the failure and dilatation criteria of gypsum at 25 °C and 110 °C in the Mogi stress space are obtained, respectively. The measurement of lateral strain indicates the dilatancy of the gypsum sample, and then the octahedral stress of the dilatancy point is best fitted to gain the dilatation criteria at 25 °C and 110 °C. The data of failure stress and dilatancy stress in the Mogi stress space can be well described in the form of a parabolic function as shown in Eq. (6), and the fitting parameters are shown in Table 2.

$$\tau^p_{oct} = A\left(\sigma^p_{m,2}\right)^2 + B\sigma^p_{m,2} + C. \tag{6}$$

Table 2 Characteristic damage stresses and deformation parameters under THM coupling

Temperature (°)	Confining (MPa)	σ_{cc} (MPa)	σ_{ci} (MPa)	σ_{cd} (MPa)	σ_s (MPa)	*E*s (GPa)	Poisson's ratio
25	5	12.32	26.28	34.87	43.11	21.04	0.25
	15	20.1	34.71	50.06	64.22	21.17	0.26
	25	32.17	43.85	58.18	70.67	23.07	0.29
	35	41.80	59.78	66.80	87.07	23.63	0.33
60	5	12.17	19.08	27.28	37.05	17.56	0.21
	35	39.43	45.86	56.71	80.91	18.17	0.25
110	5	10.45	14.21	18.43	21.63	8.76	0.14
	15	13.11	22.26	34.25	48.85	9.08	0.17
	25	27.43	38.37	45.08	67.56	10.61	0.29
	35	36.13	44.82	49.66	80.29	11.64	0.30

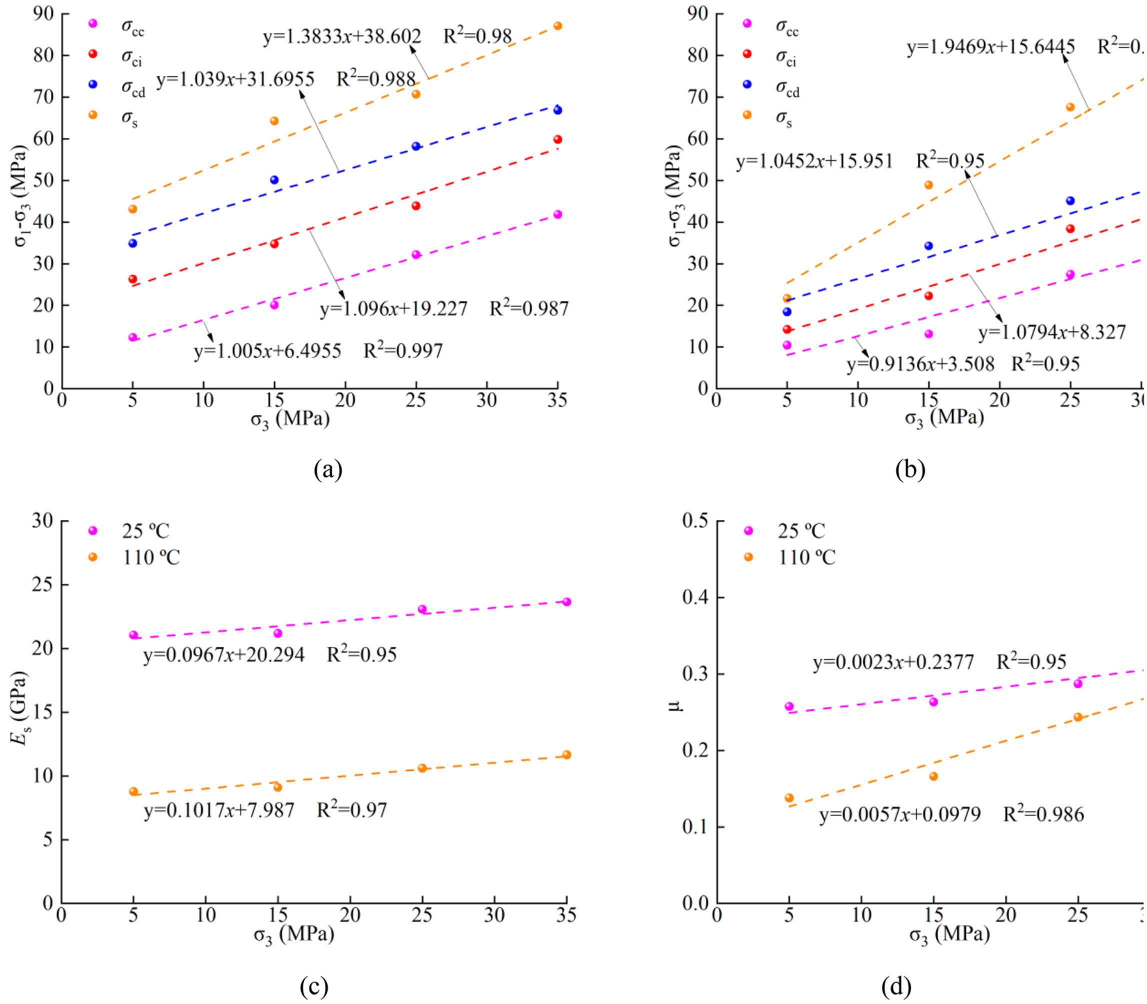

Fig. 6 Fitting of characteristic damage stresses and deformation parameters under THM coupling: **a** characteristic damage stresses at T = 25 °C; **b** characteristic damage stresses at T = 110 °C; **c** elastic modulus; **d** Poisson's ratio

When $\tau_{oct} < \tau_{oct}^{d}$ and $\tau_{oct}^{d} < \tau_{oct} < \tau_{oct}^{p}$, the gypsum sample is in compaction and dilatation stage, respectively, while the gypsum sample is in the failure stage when $\tau_{oct} < \tau_{oct}^{p}$. When gypsum transits from the compaction stage to the dilatation stage, it is necessary to pay attention to the tightness of salt cavern gas storage, and the stability of caprock should put the emphasis on the failure stage.

3.1.3 Failure Modes Under THM Coupling

There are many important factors that affect the failure type of rock, which mainly depends on rock lithology, external forces, temperature, microstructure and so on (Shengqi et al. 2017). Figure 8 reveals the failure types of gypsum samples under different temperatures and confining pressures by means of sample photos and Computed Tomography (CT) images. As shown in Fig. 8, an obvious diagonal shear fracture can be observed on gypsum samples under the confining pressure of 5 MPa at T = 25 °C (Fig. 8(a)), while the gypsum specimens show a mixed failure mode of shear (or conjugate shear) and tension with the confining pressures of 15 MPa, 25 MPa and 35 MPa (Fig. 8(b)–(d)). The gypsum samples show the phenomenon of expansion deformation with the action of axial load, and the expansion deformation increases with the increase of confining pressure. It should be noted that under higher confining pressure (σ_3 = 25 and 35 MPa), the shear failure mode of gypsum specimen is in the form of a closed shear band, which is due to the effect of high confining pressure that the shear fractures of gypsum specimen are healed. Under the confining pressure of 5 MPa at T = 60 °C (Fig. 8 (e)), the gypsum specimen failed by a mixed-mode of shear and tensile, which is different from that under the confining pressure of 5 MPa at T = 25 °C. Due to the joint action of high confining pressure and high temperature indicated in Fig. 8(f), the specimen dilatates into a final barrel shape and produces closed shear bands

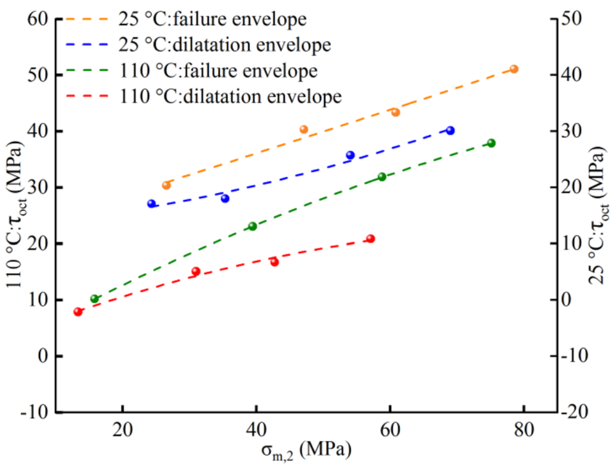

Fig. 7 Mogi failure and dilatation envelopes drawn for gypsum samples under THM coupling **a** $\sigma_3=5$ MPa and T = 25 °C **b** $\sigma_3=15$ MPa and T = 25 °C **c** $\sigma_3=25$ MPa and T = 25 °C **d** $\sigma_3=35$ MPa and T = 25 °C **e** $\sigma_3=5$ MPa and T = 60 °C **f** $\sigma_3=35$ MPa and T = 60 °C **g** $\sigma_3=5$ MPa and T = 110 °C **h** $\sigma_3=15$ MPa and T = 110 °C **i** $\sigma_3=25$ MPa and T = 110 °C

and many micro cracks. At temperature T = 110 °C, the samples are shown in Fig. 8(g)–(j) reveal that the failure mode is a shear fracture on account of the thermal expansion effect, and a closed shear band appears at confining pressure of 35 MPa. Thus, the thermal expansion effect has a healing effect at confining pressure of 35 MPa, but has a negative effect on the healing of shear cracks at confining pressure of 5—25 MPa (Chiara et al. 2020). It is mentioned in Sect. 3.1.1 that gypsum will dehydrate at 110 °C, resulting in many pores, which is also confirmed in Fig. 8(g)–(j). With the increase of confining pressure to 25 MPa and 35 MPa, the unobserved pores in the samples shown in Fig. 8(i)–(j). This is the result of the increase of confining pressure, which results in the compaction of pores produced by dehydration.

3.2 Permeability Analysis

The stress–strain curve and permeability are plotted in Fig. 9 to reveal the evolution of permeability during the whole test process under THM coupling. The evolution curves of the permeability of gypsum samples under the THM coupling has been demonstrate in Fig. 10 Using the axial strain–permeability curves demonstrated in Fig. 11, the evolution trend of permeability is presented, and the permeability decreases in both compaction and linear elastic deformation stages, which is the result of the closure of pre-existing micro-defects and newly formed microcracks under axial and confining pressures shown in Fig. 11(a). In the microcrack initiation and unstable fracture development stage, the main reason for the obvious increase of permeability is the propagation and merger of microcracks can be interpreted in Fig. 11(b), (c). In the macroscopic crack failure stage, the specimen forms a macroscopic fracture mode and forms a penetrating seepage channel along the fracture surface indicated in Fig. 11(d). At this stage, the permeability increases significantly, especially at lower confining pressures ($\sigma_3=5$ and 15 MPa), until the specimen fails. At this stage, the permeability has little change at confining pressure of 35 MPa, and slowly increases under lower confining pressure ($\sigma_3=5$ and 15 MPa) until the specimen fails. Figure 10(a), (b) reveals that under lower confining pressure ($\sigma_3=5$ and 15 MPa), the axial stress–permeability evolution curves all experienced three stages: first decrease, then rapidly increase and then develop steadily. However, the axial stress–permeability evolution curves first decrease and then continue to increase until the specimens form a macro-failure mode under higher confining pressure ($\sigma_3=25$ and 35 MPa). Under low confining pressure ($\sigma_3=5$ MPa) shown in Fig. 10(a), the increase of temperature leads to the more obvious thermal expansion effect of the specimens, and the expansion deformation of the specimens was constrained by the action of axial pressure and confining pressure (Tao et al. 2017). In the compaction and linear elastic deformation stages, the higher the temperature, the more closed the internal pores and microcracks of the specimens, resulting in fewer cracks and unstable cracks. Therefore, the higher the temperature, the lower the permeability is shown in Fig. 10(a). As discussed in Sect. 3.1.2, high temperature leads to the decrease of specimen strength, which leads to the advance of microcrack initiation and unstable fracture development stages. At T = 110 °C of 15 MPa confining pressure shown in Fig. 10(b), the permeability increased rapidly from the beginning of the microcrack initiation stage. The permeability at T = 110 °C was first lower than that at T = 25 °C, and then increased rapidly to higher than T = 25 °C, but the final permeability $k_p=1.19\times10^{-15}$ m^2, which was also lower than the permeability $k_p=1.33\times10^{-15}$ m^2 at T = 25 °C. Under the effect of lower confining pressure, the increase in temperature leads to a decrease in the final permeability of the gypsum specimens, which is confirmed in Tao's study (Tao et al. 2017). Referring to the research on rocksalt in Brodsky's study (Brodsky 1995), it can be explained that the higher the temperature under the lower confining pressure ($\sigma_3=5$ and 15 MPa), the better the healing effect of the cracks of the specimen. As analyzed in Sect. 3.1.1, under higher confining pressure ($\sigma_3=25$ and 35 MPa), with the increase of temperature, the hardening of gypsum specimens becomes more obvious, and the continuous development of cracks leads to the continuous growth of permeability. The total pore volume of samples under different confining pressures and temperatures is obtained

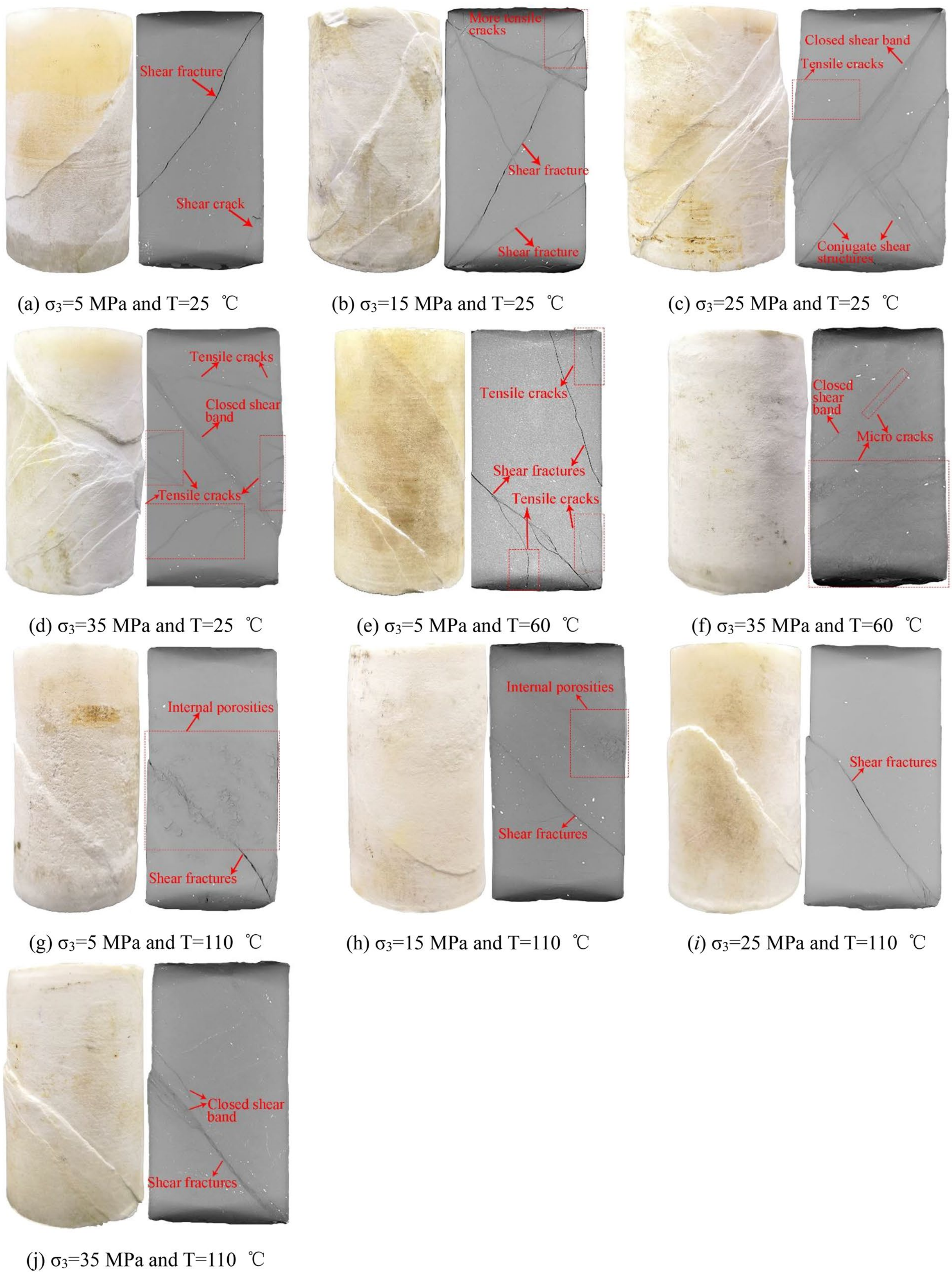

Fig. 8 Failure mode of gypsum samples under THM coupling: There is no tensile crack in the samples at t = 110 °C

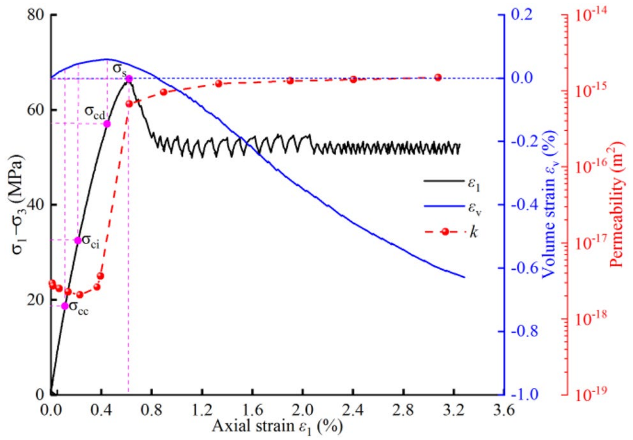

Fig. 9 The evolution of deviatoric stress, volume strain and permeability with axial strain **a** $\sigma_3=5$ MPa **b** $\sigma_3=15$ MPa **c** $\sigma_3=25$ MPa **d** $\sigma_3=35$ MPa **e** T = 25 °C **f** T = 60 °C **g** T = 110 °C

by three-dimensional space analysis of the cracks by CT scanning as indicated in Fig. 12. The total pore volume of the samples are shown in Table 3, which decreases with the increase of temperature under lower confining pressure ($\sigma_3=5$ and 15 MPa) and increases with the increase of temperature under higher confining pressure ($\sigma_3=25$ and 35 MPa). It has been confirmed in Zhang's study (Zhang et al. 2020) that the permeability of rock is directly proportional to the total pore volume.

To analyze the influence of confining pressure on gypsum permeability under THM coupling, the axial strain–permeability evolution curves (Table 4) under different confining pressures at different temperatures are drawn in Fig. 10(e)–(g). The variation of permeability is closely related to confining pressure, because the increase of confining pressure is conducive to the closure of internal pores and microcracks, which leads to the decrease of permeability. The variation of permeability with confining pressure is consistent with the variation of total pore volume. Figure 13 reveals the relationship between permeability and confining pressure by fitting the permeability of different confining pressures at T = 25 and 60 °C to obtain the best fitting curves, which can be expressed as two exponential functions.

At 25 °C:

$$k_p^{T=25\,^\circ C} = 75.97 \times 0.764^{\sigma_3} \times 10^{-15}\ R^2 = 1 \tag{7}$$

At 110 °C:

$$k_p^{T=110\,^\circ C} = 8.1557 \times 0.88^{\sigma_3} \times 10^{-15}\ R^2 = 0.99993 \tag{8}$$

where $k_p^{T=25\,^\circ C}$ and $k_p^{T=110\,^\circ C}$ are the final permeability at T = 25 and 110 °C, respectively. According to the best fitting curves, the permeability decreases with the increase of confining pressure, and the decreasing rate also decreases gradually.

3.3 AE Ringing Count and Energy Characteristic Parameters

Acoustic emission (AE) technology can be employed to reveal the microcrack initiation and propagation in rocks, which contributes to demonstrate the characteristics of the whole process of rock fracture (Wang et al. 2017; Zhang et al. 2019; Zhao et al. 2020). The evolution curves of AE ring count, axial stress, cumulative AE ring counts, cumulative energy and time are plotted in Fig. 14 and Fig. 15 to investigate the AE characteristics of gypsum specimens under THM coupling.

According to Fig. 14, the variation characteristics of AE ringing count with the time of gypsum specimen under the same confining pressure are fundamentally similar. When $\sigma_3=5$ and 15 MPa, the AE ringing counts are less in the initial stage of axial compression loading, which indicates that there are fewer closed microcracks in this stage. With the increase of axial compression loading, the formation and propagation of cracks lead to the increase of AE ringing count. Near the peak stress, the gypsum specimen is close to failure, and the AE ring count reaches the maximum value of 256.3 times/ s. Moreover, in the residual strain stage, the AE ring count shows decreasing trends. Figure 14(c), (h) shows that the AE ring counts of gypsum specimens with $\sigma_3=25$ MPa increase first and then decrease, and they are also less in the initial loading stage and the anaphase of failure. It is noteworthy that at $\sigma_3=35$ MPa, AE ringing count increases with time, and the maximum value appears in the anaphase of plastic deformation. Owing to the constrain of confining pressure, there are few microcracks formed in gypsum specimens, and the AE activity, cumulative AE ring counts and cumulative energy decrease with the increase of confining pressure at the same temperature shown in Figs. 14 and 15, which also explains the reason why the permeability decreases with the increase of confining pressure. Besides, the peaks of AE ring count and axial stress curves have an obvious hysteresis effect with the increase of confining pressure.

When the confining pressure is constant, the AE activity, cumulative AE ring counts and cumulative energy decrease with the increase of temperature, and the peaks of AE ring count also shows an obvious hysteresis effect. What's interesting is that under the confining pressure of 35 MPa, the maximum value of AE ringing count increases with the increase of temperature, which demonstrates the higher the temperature in the anaphase of deformation, the greater the deformation. Figure 15 shows the evolution curves of cumulative AE ring count and cumulative energy with time, and

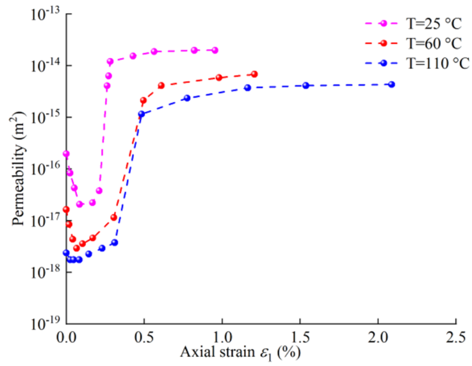

(a) σ3 =5 MPa

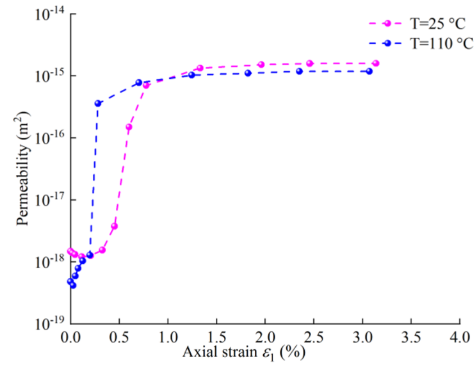

(b) σ3=15 MPa

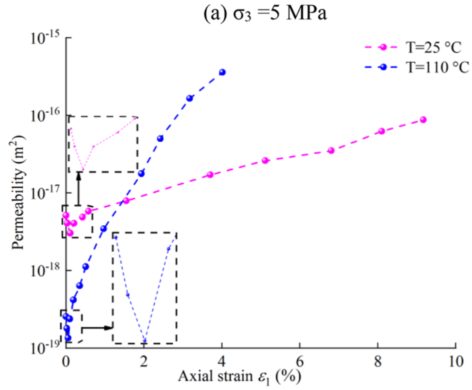

(c) σ3=25 MPa

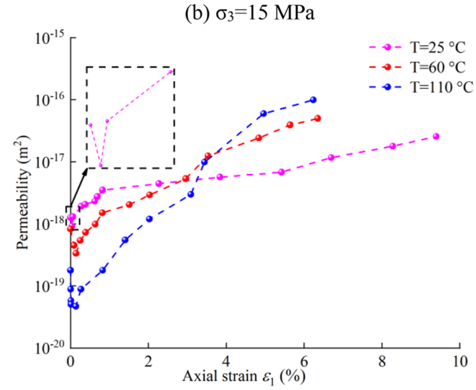

(d) σ3=35 MPa

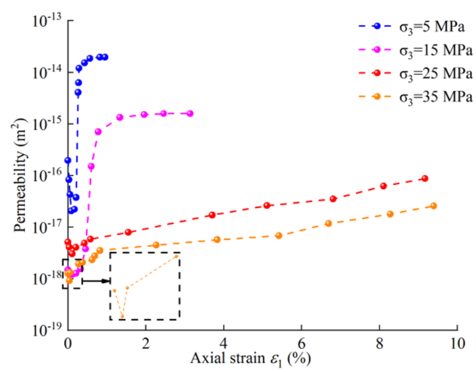

(e) T=25 ℃

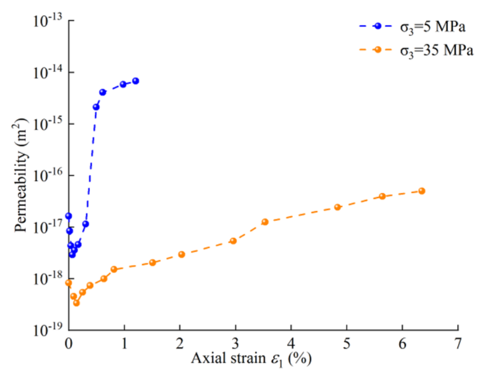

(f) T=60 ℃

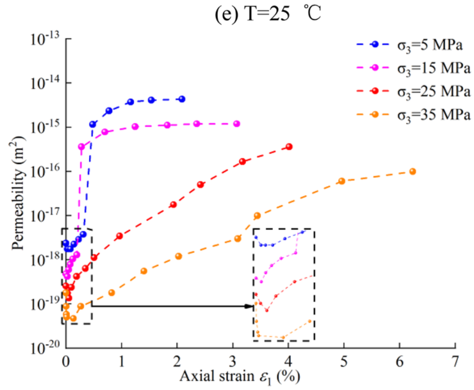

(g) T=110 ℃

Fig. 10 The evolution curves of axial strain–permeability under THM coupling: When the temperature increases, the permeability of the samples under the confining pressure $\sigma_3 = 5$ MPa decreases, while the permeability of the samples under the confining pressure $\sigma_3 = 15$, 25 and 35 MPa increases. The increase in confining pressure inhibits the increase in the permeability of the samples. **a** Compaction and linear elastic deformation **b** microcrack initiation **c** unstable crack growth **d** macroscopic crack failure

the variation trend of both is basically consistent. Although AE activity is lower at high temperature at $\sigma_3 = 35$ MPa, more seepage channels are formed due to dehydration reaction, and the higher the temperature is, the greater the final permeability of the gypsum specimen is.

4 Discussion

In this work, the mechanical properties, permeability and acoustic emission characteristics of gypsum are revealed through THM coupling experiment. The permeability medium in the previous studies is CO_2, while the permeability medium in this experiment is nitrogen, which will not react with the sample to generate new substances, which can more truly reflect the physical and mechanical properties of gypsum caprock for salt cavern oil/gas storage (Hangx et al. 2011). The research on the strength of gypsum caprock has attracted considerable attention, and we have collected a number of experimental data, which are plotted in Fig. 16 for comparison (De Paola et al. 2009; Hangx et al. 2010; Hangx et al. 2011; J et al. 1957; Liang et al. 2007; Müller 1974; Hansen and Pfeifle 1998; Sampaleanu 2010). Although the evolution trend of peak strength of gypsum caprock with confining pressure is the same, the difference between different results can reach about 70% (Hangx et al. 2011; J et al. 1957). It emphasizes the importance of using data for specific location when predicting caprock stability. Our research team conducted a series of THM coupling tests on different types of caprock from the same salt cavern oil/gas storage, including gypsum, dolomite and limestone. To analyze the difference between the mechanical properties and permeability of different types of caprock, the peak strength and permeability of three different types of caprock are presented in Figs. 17 and 18, respectively (Xu et al. 2020; Zhang et al. 2019). The evolution trend of peak strength with confining pressure can be well described by linear function. Figure 17 reveals that the peak strength of gypsum is significantly lower than that of dolomite and limestone, because gypsum is soft rock and dolomite and limestone are hard rock. The increase of confining pressure can result in the increase of permeability in caprock, and the permeability of limestone at 110 °C is the lowest. The permeability of gypsum at T = 25 °C is higher than that of limestone, while the permeability of gypsum at T = 110 °C is lower than that of dolomite. In different types of caprock, there are significant differences in permeability. Therefore, employing data from specific locations and specific caprocks to predict and evaluate the stability of caprock is an important prerequisite for ensuring the safety of salt cavern storage.

Due to experimental conditions, the maximum temperature of this experiment is 110 °C. When the temperature is higher (T > 110 °C) under THM coupling, the evolution of permeability of gypsum caprock needs to be explored. The influence of dehydration reaction progress on the evolution of permeability of gypsum samples under THM coupling needs to be further conducted.

5 Conclusions

Investigating the mechanical properties, permeability and acoustic emission characteristics of gypsum under THM coupling is conducive to optimize the design of salt cavern gas storage to ensure its tightness and stability, and can also guide the application of gypsum in the construction industry. Detailed analysis and discussion of the experimental results can obtain the following main conclusions:

(1) The full stress–strain curves of gypsum samples experience compaction, linear elastic deformation, microcrack initiation, unstable crack growth, and macroscopic crack failure stages under THM coupling. The peak strength of gypsum decreases with the increase of temperature and increases with the increase of confining pressure, the failure criterion and dilatation criterion of gypsum at 25 °C and 110 °C are obtained based on the Mogi failure criterion, respectively.

(2) The failure modes of gypsum specimens under lower confining pressure ($\sigma_3 = 5$ MPa and 15 MPa) at 25 °C and 60 °C show shear fracture or a mixed-mode of shear and tensile, and shear failure at 110 °C. The increase of confining pressure and temperature can increase the expansion deformation of gypsum specimens. Higher confining pressure ($\sigma_3 = 25$ MPa and 35 MPa) has a positive effect on fracture healing, while high temperature has a negative effect on fracture healing under high confining pressure due to the thermal expansion effect. Many pores can be formed on account of dehydration reaction, but they are compacted with the increase of confining pressure.

(3) In the compaction and linear elastic deformation stage, the higher the temperature is, the lower the permeability is, and the final permeability is closely related to the confining pressure and failure type. When $\sigma_3 = 5$ MPa and 15 MPa, the final permeability decreases with the increase of temperature, but increases with the increase of temperature under the higher confining pressure ($\sigma_3 = 25$ MPa and 35 MPa). The increase of confining pressure inhibits the formation of microcracks and pores, resulting in a decrease

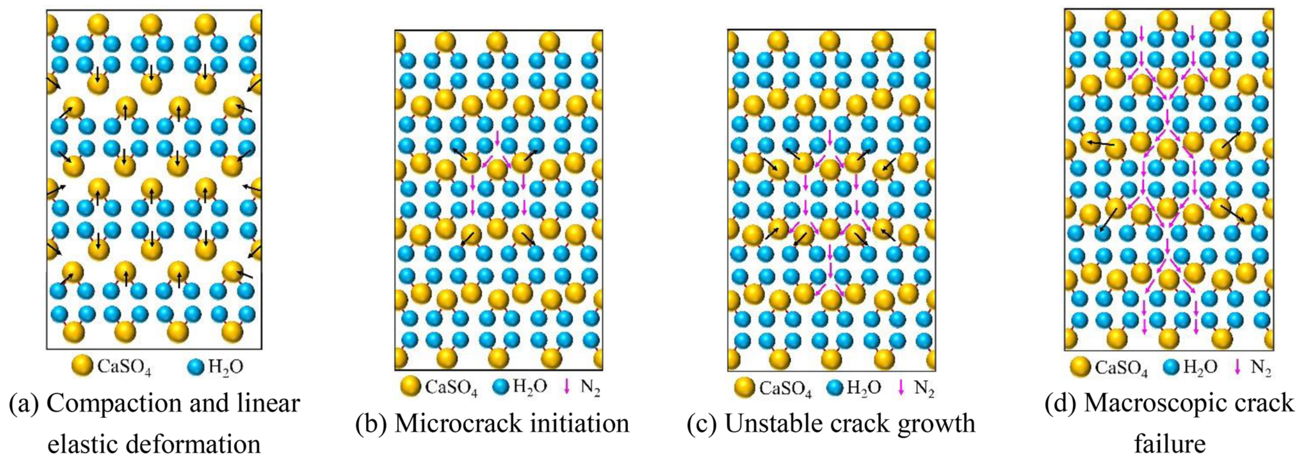

Fig. 11 Penetration of gypsum samples at different stages

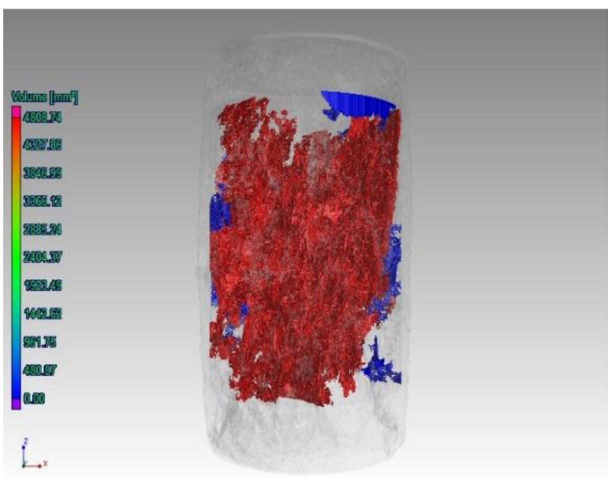

Fig. 12 3D space analysis by CT scanning

Table 3 Fitting parameters of failure stress and dilatancy stress data in Mogi stress space

Stress data (MPa)	Temperature (°C)	A	B	C	R^2
Failure stress	25	0.000102	0.377	10.8294	0.986
	110	− 0.0022	0.668	0.1736	0.999
Dilatancy stress	25	0.00232	0.0945	12.8719	0.979
	110	− 0.00262	0.4689	2.4202	0.984

of permeability, and the best fitting formulas of the relationship between permeability and confining pressure are given at 25 °C and 110 °C

(4) The AE activity is inhibited by the increase of confining pressure and temperature by analyzed AE ring count, cumulative AE ring counts and energy, and the AE peaks

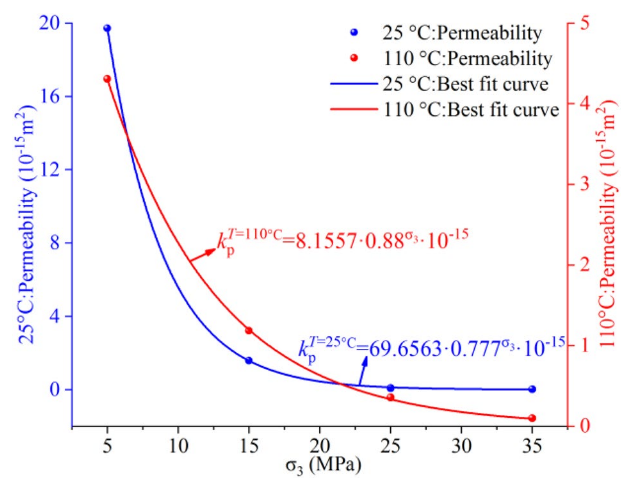

Fig. 13 The relationship between permeability and confining pressure under THM coupling **a** $\sigma_3=5$ MPa and T = 25 °C **b** $\sigma_3=15$ MPa and T = 25 °C **c** $\sigma_3=25$ MPa and T = 25 °C **d** $\sigma_3=35$ MPa and T = 25 °C **e** $\sigma_3=5$ MPa and T = 60 °C **f** $\sigma_3=35$ MPa and T = 60 °C **g** $\sigma_3=5$ MPa and T = 110 °C **h** $\sigma_3=15$ MPa and T = 110 °C **i** $\sigma_3=25$ MPa and T = 110 °C **j** $\sigma_3=35$ MPa and T = 110 °C

Table 4 Cracking analysis under THM coupling

	Temperature (°C)	$\sigma_3=5$ MPa	$\sigma_3=15$ MPa	$\sigma_3=25$ MPa	$\sigma_3=35$ MPa
Total pore volume (mm^3)	25	5214	4671	2335	2137
	60	4627			2635
	110	3819	3625	3365	3017

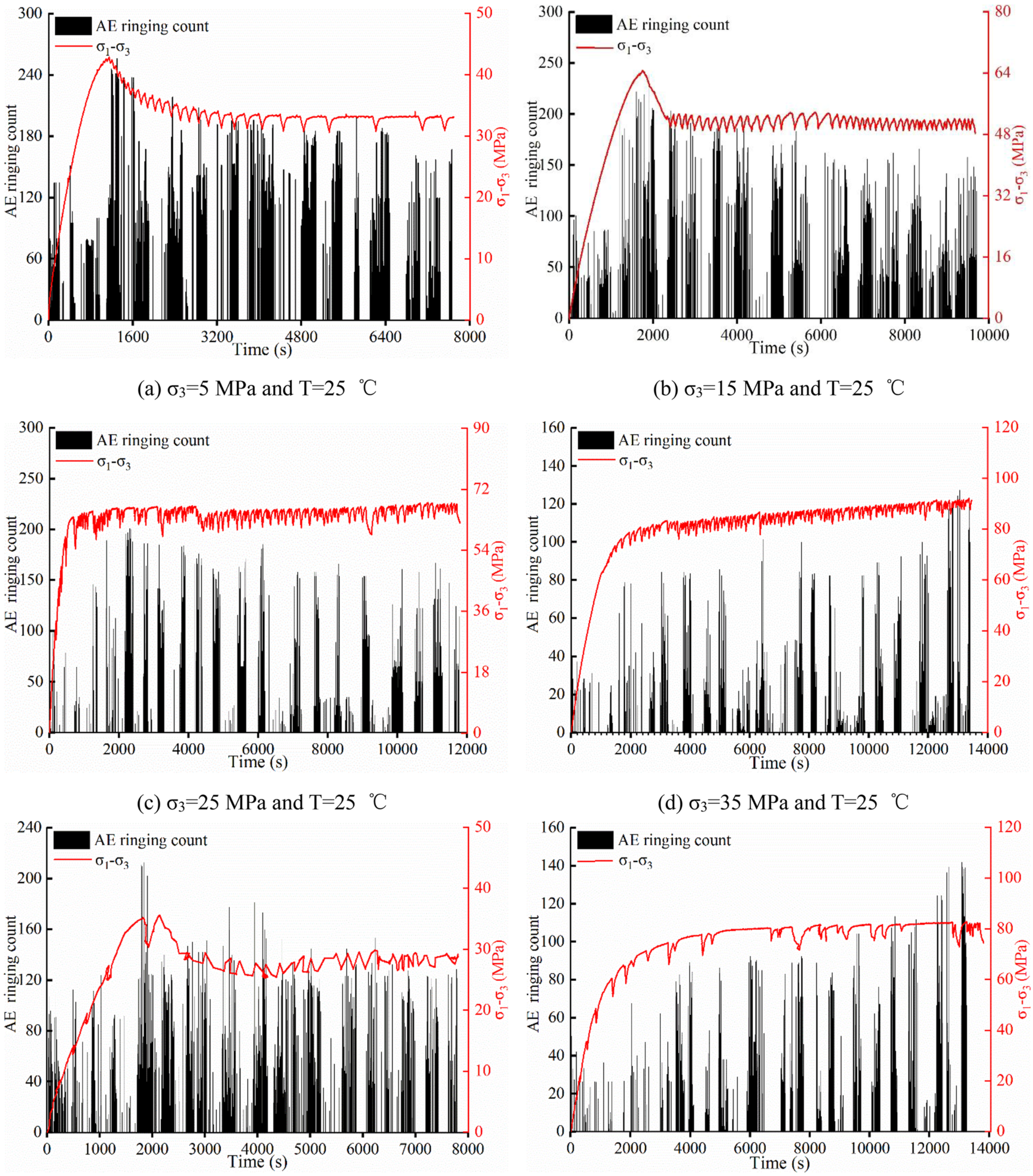

(a) σ3=5 MPa and T=25 ℃

(b) σ3=15 MPa and T=25 ℃

(c) σ3=25 MPa and T=25 ℃

(d) σ3=35 MPa and T=25 ℃

(e) σ3=5 MPa and T=60 ℃

(f) σ3=35 MPa and T=60 ℃

Fig. 14 Stress–time–AE curves of gypsum samples under THM coupling: Peaks of AE ringing count and deviator stress appear almost simultaneously **a** $\sigma_3 = 5$ MPa **b** $\sigma_3 = 15$ MPa **c** $\sigma_3 = 25$ MPa **d** $\sigma_3 = 35$ MPa

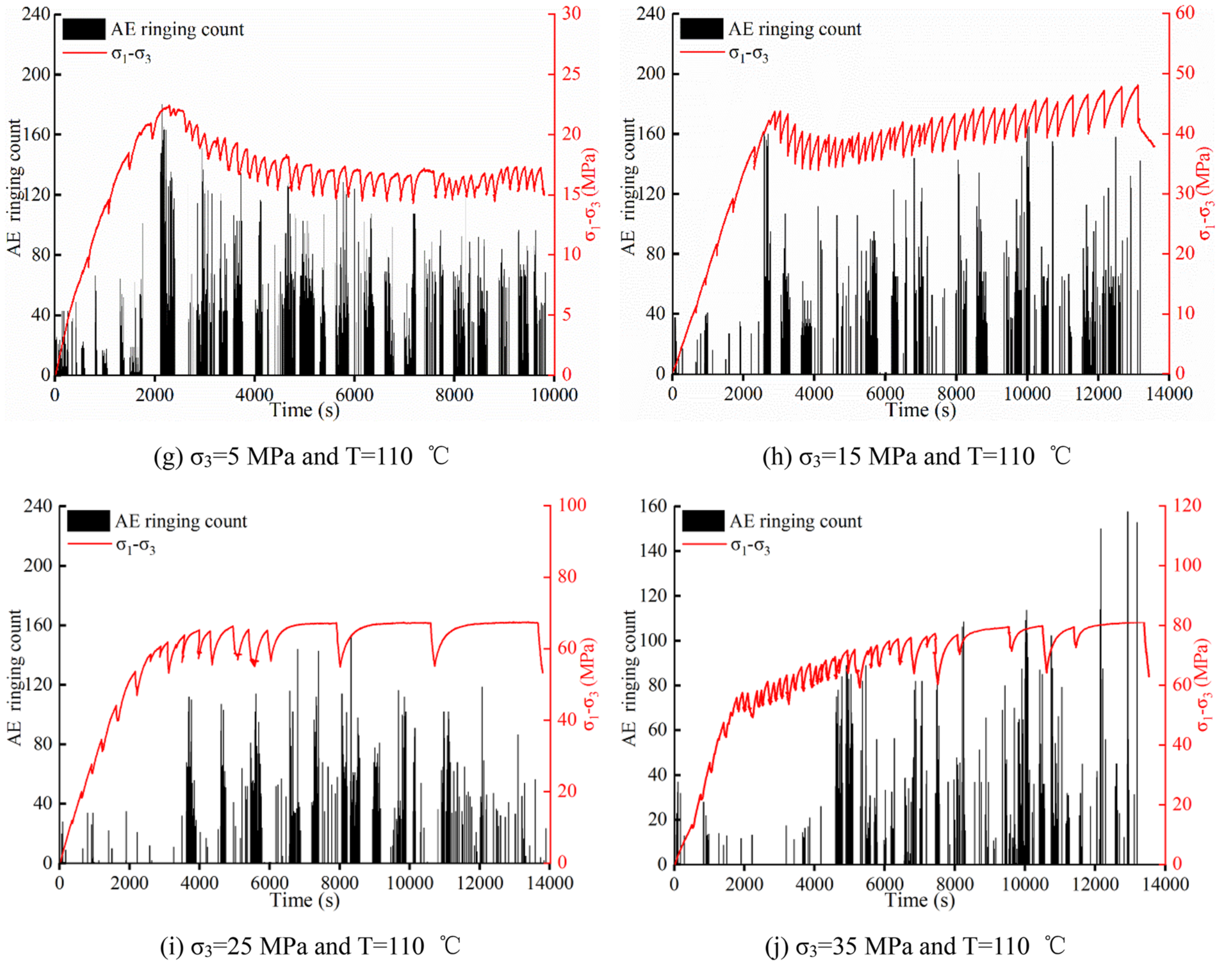

(g) σ_3=5 MPa and T=110 ℃

(h) σ_3=15 MPa and T=110 ℃

(i) σ_3=25 MPa and T=110 ℃

(j) σ_3=35 MPa and T=110 ℃

Fig. 14 (continued)

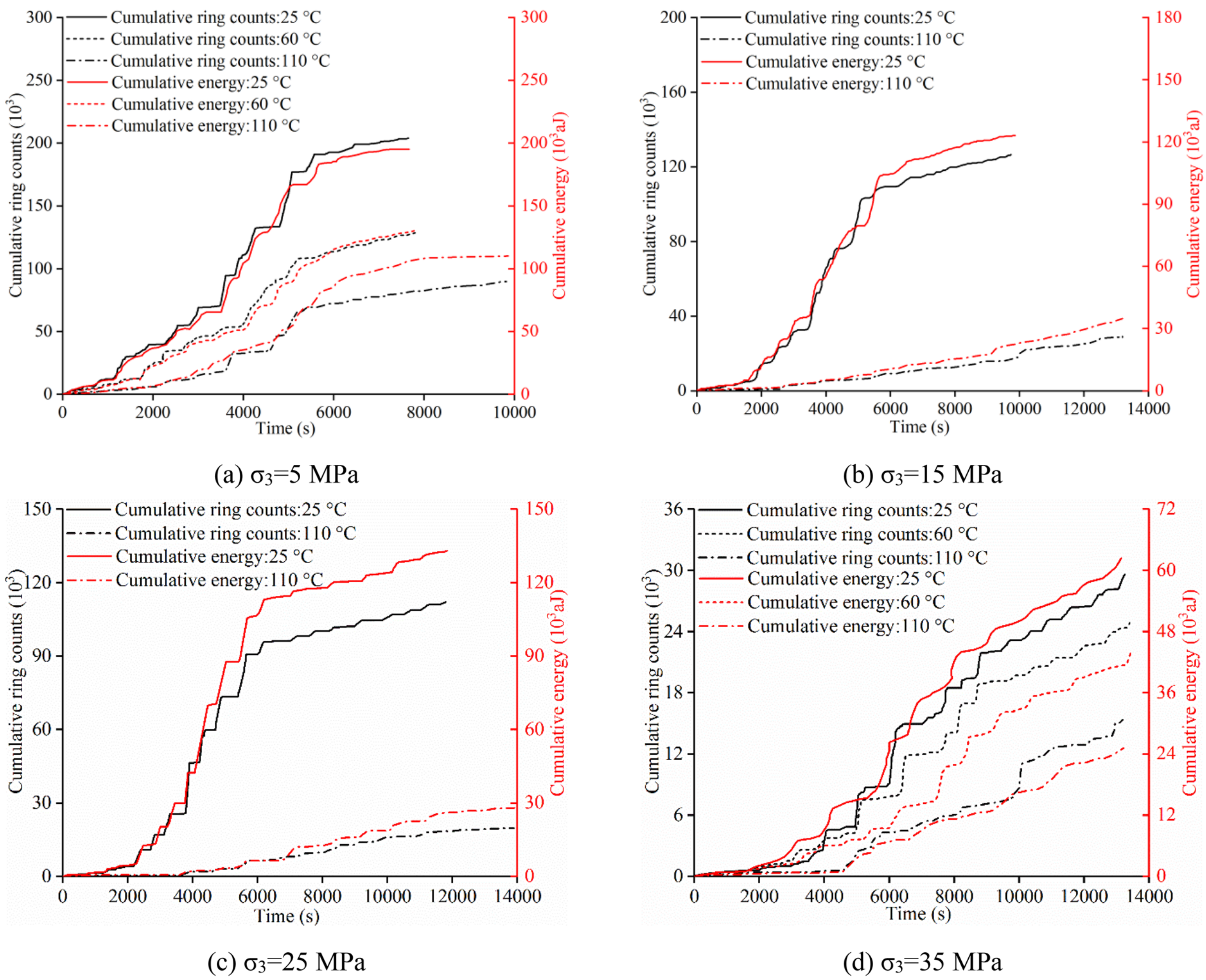

Fig. 15 Cumulative ring counts and cumulative energy under THM coupling

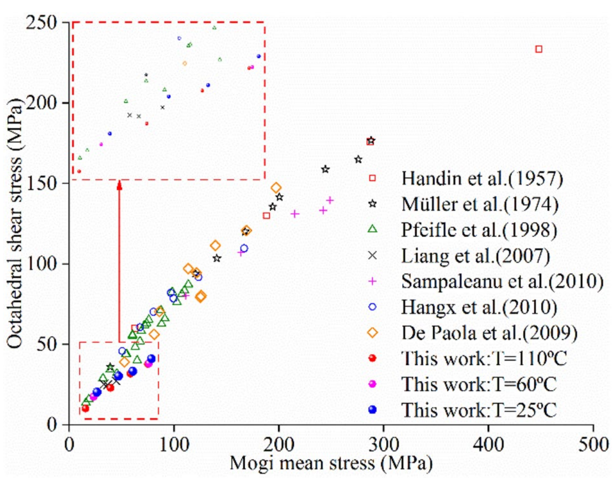

Fig. 16 Comparison of octahedral shear stress of gypsum caprock

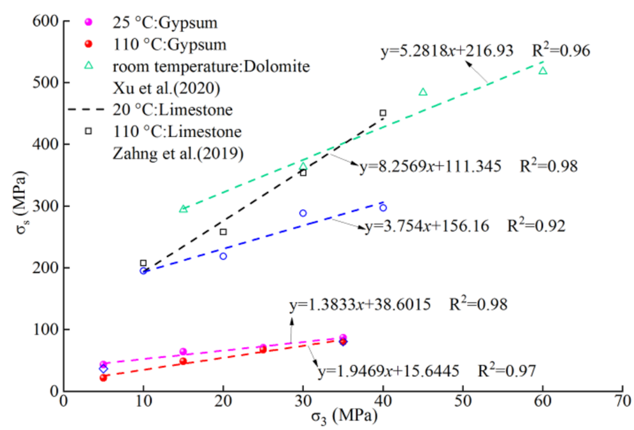

Fig. 17 Comparison of peak failure strength of different types of caprock

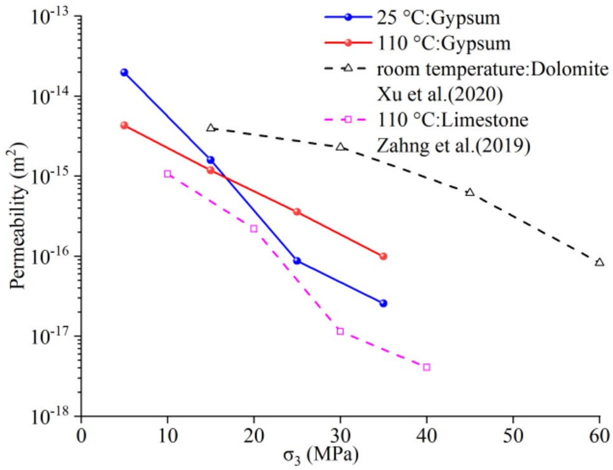

Fig. 18 Comparison of permeability of different types of caprock

have the same hysteresis effect as the stress peaks. However, it should be noted that the peaks of AE ring count increase with the increase of temperature in the anaphase of deformation.

Acknowledgements This research was financially supported by the National Natural Science Foundation of China (Grant No. U20A20266, 51874202) and Major Talent Projects, and the Ten Thousands Plan Youth Top Project proposed by the Organization Department of the Central Committee of the CPC.

Declarations

Conflicts of Interest The authors declare that the work described has not been published before; that it is not under consideration for publication anywhere else; that its publication has been approved by all co-authors; that there is no conflict of interest regarding the publication of this article.

References

Brace WF, Walsh J, Frangos W (1968) Permeability of granite under high pressure. J Geophys Res 73:2225–2236

Brantut N, Schubnel A, Guéguen Y (2011) Damage and rupture dynamics at the brittle-ductile transition: the case of gypsum. J Geophys Res: Solid Earth. https://doi.org/10.1029/2010JB007675

Brantut N, Schubnel A, David EC et al (2012) Dehydration-induced damage and deformation in gypsum and implications for subduction zone processes. J Geophys Res: Solid Earth. https://doi.org/10.1029/2011jb008730

Brodsky NS, Munson DE (1994) Thermomechanical damage recovery parameters for rock salt from the waste isolation pilot plant. In: Nelson PP, Laubach SE (eds) Proc. First N. Amer. Rock Mech. Symp., Balkema, Brookfield, VT, pp 731–738

Cai MKPK, Tasaka Y et al (2004) Generalized crack initiation and crack damage stress thresholds of brittle rock masses near underground excavations. Int J Rock Mech Min Sci 41:833–847. https://doi.org/10.1016/j.ijrmms.2004.02.001

Chaki S, Takarli M, Agbodjan WP (2008) Influence of thermal damage on physical properties of a granite rock: porosity, permeability and ultrasonic wave evolutions. Constr Build Mater 22:1456–1461. https://doi.org/10.1016/j.conbuildmat.2007.04.002

Changbao Jiang MD, Guangzhi Yin JG, Wang TL, Jiang Xu, Zhang D, Huang G (2017) Experimental study on seepage properties, AE characteristics and energy dissipation of coal under tiered cyclic loading. Eng Geol. https://doi.org/10.1016/j.enggeo.2017.03.005

Chen D, Wang E-y, Li N (2017) Analyzing the rules of fracture and damage, and the characteristics of the acoustic emission signal of a gypsum specimen under uniaxial loading. J Geophys Eng 14:780–791. https://doi.org/10.1088/1742-2140/aa676e

Chiara C, Sabrina Maria Rita B, Daniele C (2020) Crack coalescence and strain accommodation in gypsum rock. Frattura Ed Integrità Strutturale 14:247–255. https://doi.org/10.3221/igf-esis.52.19

De Paola N, Faulkner D, Collettini C (2009) Brittle versus ductile deformation as the main control on the transport properties of low-porosity anhydrite rocks. J Geophys Res: Solid Earth. https://doi.org/10.1029/2008JB005967

Feng XT, Haimson B, Li X et al (2019) ISRM suggested method: determining deformation and failure characteristics of rocks subjected to true triaxial compression. Rock Mech Rock Eng 52(6):2011–2020

Hangx SJTSCJ, Peach CJ (2011) The mechanical behavior of anhydrite and the effect of deformation on permeability development-Implications for caprock integrity during geological storage of CO2. Energy Procedia 4:5358–5363. https://doi.org/10.1016/j.egypro.2011.02.518

Hangx SJT, Spiers CJ, Peach CJ (2010) Mechanical behavior of anhydrite caprock and implications for CO2sealing capacity. J Geophys Res. https://doi.org/10.1029/2009jb006954

Hangx SJT, Spiers CJ, Peach CJ (2011) The mechanical behavior of anhydrite and the effect of deformation on permeability development–Implications for caprock integrity during geological storage of CO2. Energy Procedia 4:5358–5363. https://doi.org/10.1016/j.egypro.2011.02.518

Hansen FD, Pfeifle TW (1998) Database of mechanical and hydrological properties of WIPP Anhydrite derived from laboratory-scale experiments. Sandia National Laboratories, Albuquerque, Livermore

Hoxha D, Homand F, Auvray C (2006) Deformation of natural gypsum rock: Mechanisms and questions. Eng Geol 86:1–17. https://doi.org/10.1016/j.enggeo.2006.04.002

Iucolano F, Liguori B, Aprea P et al (2018) Thermo-mechanical behaviour of hemp fibers-reinforced gypsum plasters. Constr Build Mater 185:256–263. https://doi.org/10.1016/j.conbuildmat.2018.07.036

J H, RV H (1957) Experimental deformation of sedimentary rocks under confining pressure: tests at room temperature on dry samples. Bull Am Assoc Petrol Geol 41:1–50

Ko SODL (1995) The transition from weakening to strengthening in dehydrating gypsum: evolution of excess pore pressures. Geophys Res Lett 22:1009–1012

Leclère H, Faulkner D, Llana-Fúnez S et al (2018) Reaction fronts, permeability and fluid pressure development during dehydration reactions. Earth Planet Sci Lett 496:227–237. https://doi.org/10.1016/j.epsl.2018.05.005

Liang W-g, Yang C-h, Zhao Y-s et al (2007) Experimental investigation of mechanical properties of bedded salt rock. Int J Rock Mech Min Sci 44:400–411

Lockner D (1993) The role of acoustic emission in the study of rock fracture. Int J Rock Mech Min Sci 30(7):883–899

Menéndez B, David C (2012) The influence of environmental conditions on weathering of porous rocks by gypsum: a non-destructive study using acoustic emissions. Environmental Earth Sciences 68:1691–1706. https://doi.org/10.1007/s12665-012-1861-2

Meng Q, Zhang M, Han L et al (2018) Acoustic emission characteristics of red sandstone specimens under uniaxial cyclic loading and unloading compression. Rock Mech Rock Eng 51:969–988. https://doi.org/10.1007/s00603-017-1389-6

Milsch H, Priegnitz M, Blöcher G (2011) Permeability of gypsum samples dehydrated in air. Geophys Res Letters. https://doi.org/10.1029/2011gl048797

Mirwald PW (2008) Experimental study of the dehydration reactions gypsum-bassanite and bassanite-anhydrite at high pressure: indication of anomalous behavior of H(2)O at high pressure in the temperature range of 50–300 degrees C. J Chem Phys 128:074502. https://doi.org/10.1063/1.2826321

Mogi K (1971) Fracture and flow of rocks under high triaxial compression. J Geophys Res 76:1255–1269. https://doi.org/10.1029/JB076i005p01255

Müller PSHF (1974) Verformbarkeit und gefigeregelung von anhydrit experimentelle stauchverformung unter manteldrucken bis 5 kbar bei temperaturen bis 300°C. Tectonophysics 23:105–127

Olgaard DL, Ko S-c, Wong T-f (1995) Deformation and pore pressure in dehydrating gypsum under transiently drained conditions. Tectonophysics 245:237–248

Sampaleanu C (2010) Mechanical strength of anhydrite and its role in the seismicity of the Duke River Fault, Yukon Territory. B.Sc. (Honours) dissertation, University of British Columbia

Sarkar PK, Mitra N (2019) Gypsum under tensile loading: A molecular dynamics study. Constr Build Mater 201:1–10. https://doi.org/10.1016/j.conbuildmat.2018.12.097

Scholz C (1968) Experimental study of the fracturing process in brittle rock. J Geophys Res 73:1447–1454

Shengqi Y, Peng X, Yanbao L et al (2017) Experimental investigation on triaxial mechanical and permeability behavior of sandstone after exposure to different high temperature treatments. Geothermics 69:93–109. https://doi.org/10.1016/j.geothermics.2017.04.009

Strydom CAH-LDL, Potgieter JH, Dagg E (1995) The thermal dehydration of synthetic gypsum. Thermochim Acta 269:631–638

Tao M, Yechao Y, Jie C et al (2017) Investigation on the permeability evolution of gypsum interlayer under high temperature and triaxial pressure. Rock Mech Rock Eng 50:2059–2069. https://doi.org/10.1007/s00603-017-1222-2

Wang T, Ma H, Yang C et al (2015) Gas seepage around bedded salt cavern gas storage. J Natural Gas Sci Eng 26:61–71. https://doi.org/10.1016/j.jngse.2015.05.031

Wang X, Wen Z, Jiang Y et al (2017) Experimental study on mechanical and acoustic emission characteristics of rock-like material under non-uniformly distributed loads. Rock Mech Rock Eng 51:729–745. https://doi.org/10.1007/s00603-017-1363-3

Wang B, Lin R, Liu D et al (2019a) Investigation of the effect of humidity at both electrode on the performance of PEMFC using orthogonal test method. Int J Hydrogen Energy 44:13737–13743. https://doi.org/10.1016/j.ijhydene.2019.03.139

Wang C, Liu J, Wang L (2019b) Damage evolution characteristics of rock salt under different stress conditions. Advances in Civil Engineering 2019:1–12. https://doi.org/10.1155/2019/3073975

Wang H, Wu T, Fu X et al (2019c) Quantitative determination of the brittle–ductile transition characteristics of caprocks and its geological significance in the Kuqa depression Tarim Basin, Western China. J Petroleum Sci Eng 173:492–500. https://doi.org/10.1016/j.petrol.2018.10.042

Wang Y, Han JQ, Li CH (2020) Acoustic emission and CT investigation on fracture evolution of granite containing two flaws subjected to freeze–thaw and cyclic uniaxial increasing-amplitude loading conditions. Constr Build Mater. https://doi.org/10.1016/j.conbuildmat.2020.119769

Wei J, Zhu W, Guan K et al (2019) An acoustic emission data-driven model to simulate rock failure process. Rock Mech Rock Eng 53:1605–1621. https://doi.org/10.1007/s00603-019-01994-3

Wei S, Wang C, Yang Y et al (2020) Physical and mechanical properties of gypsum-like rock materials. Adv Civil Eng 2020:1–17. https://doi.org/10.1155/2020/3703706

Xu D, Liu J, Wu Z et al (2020) Experimental investigation on permeability evolution of dolomite caprock under triaxial compression. Energies. https://doi.org/10.3390/en13246535

Yang S-Q, Jing H-W, Wang S-Y (2012) Experimental investigation on the strength, deformability, failure behavior and acoustic emission locations of red sandstone under triaxial compression. Rock Mech Rock Eng 45:583–606. https://doi.org/10.1007/s00603-011-0208-8

Yunpeng H, Mingnian W, Zhilong W, Qiling W, Dagang L (2020) Mechanical behavior and constitutive model of shotcrete–rock interface subjected to heat damage and variable temperature curing conditions. Constr Build Mater 263:120171. https://doi.org/10.1016/j.conbuildmat.2020.120171

Zang ACWF, Stanchits S et al (1998) Source analysis of acoustic emissions in Aue granite cores under symmetric and asymmetric compressive loads. Geophys J Int 135:1113–1130

Zhang Q, Liu J, Xu H et al (2019) Experimental investigation on permeability evolution of limestone caprock under coupled THM processes. KSCE J Civ Eng 23:5090–5097

Zhang Q, Liu J, Wang L et al (2020) Impurity effects on the mechanical properties and permeability characteristics of salt rock. Energies. https://doi.org/10.3390/en13061366

Zhao X, Xu L, Fang C et al (2018) Study on voltage clamping and self-humidification effects of pem fuel cell system with dual recirculation based on orthogonal test method. Int J Hydrogen Energy 43:16268–16278. https://doi.org/10.1016/j.ijhydene.2018.06.172

Zhao K, Yu X, Zhu S et al (2020) Acoustic emission fractal characteristics and mechanical damage mechanism of cemented paste backfill prepared with tantalum niobium mine tailings. Constr Build Mater. https://doi.org/10.1016/j.conbuildmat.2020.119720

Zhou HW, Wang ZH, Ren WG et al (2019) Acoustic emission based mechanical behaviors of Beishan granite under conventional triaxial compression and hydro-mechanical coupling tests. Int J Rock Mech Min Sci 123:104125. https://doi.org/10.1016/j.ijrmms.2019.104125

Zhou HW, Wang XY, Zhang L et al (2020) Permeability evolution of deep coal samples subjected to energy-based damage variable. J Natural Gas Sci Eng. https://doi.org/10.1016/j.jngse.2019.103070